Earth and Planetary Science Letters 568 (2021) 117031

Contents lists available at ScienceDirect

Earth and Planetary Science Letters

www.elsevier.com/locate/epsl

# Dating individual several-km lunar impact craters from the rim annulus in region of planned Chang'E-5 landing: Poisson age-likelihood calculation for a buffered crater counting area

G.G. Michael [a], Z. Yue [b,c,*], S. Gou [b,d], K. Di [b,c]

[a] Planetary Sciences and Remote Sensing, Institute of Geological Sciences, Freie Universitaet Berlin, Malteser Strasse 74-100, Haus D, Berlin 12249, Germany
[b] State Key Laboratory of Remote Sensing Science, Aerospace Information Research Institute, Chinese Academy of Sciences, Beijing 100101, China
[c] CAS Center for Excellence in Comparative Planetology, Hefei 230026, China
[d] State Key Laboratory of Lunar and Planetary Sciences, Macau University of Science and Technology, Macau, China

ARTICLE INFO

*Article history:*
Received 26 October 2020
Received in revised form 25 May 2021
Accepted 26 May 2021
Available online xxxx
Editor: W.B. McKinnon

*Keywords:*
Chang'E-5
buffered crater counting
chronology
Poisson statistics
Oceanus Procellarum

ABSTRACT

The CE-5 lander was designed to retrieve a 2 m core of regolith for return to Earth. We attempt to date the most significant impact craters in the region of its landing using the statistics of superposed craters, anticipating the possibility of the presence of impact ejecta in the soil sample. The craters formed after the mare surface and would have made significant mass contributions across the region so that, if ejecta components can be recognised and dated by radioisotope methods, there is the potential to establish links to source craters.

The seven largest craters in the region range in size from 3–6 km, and we attempt to date them using the annulus method first proposed by Baldwin (1985). A unit covering most of the vicinity is estimated to be 3.3 Ga old, so that we expect the seven craters to be randomly spaced over this time interval. Superposed craters in the size range 20-80 m within an annulus around the craters' rims suggest ages of <50 Ma in all cases. We interpret that these times reflect the lifetime only of structures in the upper 20 m of regolith. The population of superposed craters >250 m in diameter, however, is shown to be consistent with the age of the unit, and is thus also able to provide information on the age of individual several-km craters.

The age likelihood method based on Poisson statistics, which maximises the timing information that can be obtained from small-area crater populations, is extended to cover so-called buffered crater counts. Although, in this study, we are only able to constrain the ages of the selected craters to a limited degree, the method is generally applicable to buffered counts and should substantially improve their precision elsewhere.



## 1. Introduction

The China National Space Administration's Chang'E-5 lunar sample return mission successfully landed in Oceanus Procellarum, in the northern vicinity of Mons Rümker. The spacecraft was designed to retrieve a drill core of up to 2 m depth, making up a total soil sample of around 2 kg, and return it to Earth (Zou and Li, 2017). A zone of roughly 600 × 125 km was considered for siting the landing (Zhao et al., 2016). Having an interest to anticipate what components may be found in the sample, we attempt to date the largest craters in the vicinity, the ejecta of which may be present throughout the region and include heated or melted components which could potentially be linked back to the source crater through radioisotope measurements.

The usual way to date surface features requires selecting an appropriate area, which should have been erased of its crater population by the process of formation, and measuring the accumulation of impact craters since then. In general, this is easier to achieve for features of greater areal extent because the characteristics of the accumulating population are better captured. Depending on their scale, impact craters have variously been dated by examining their floors (Kirchoff et al., 2013), ejecta – especially on Mars, where they can be more distinct as fluidized flows with distinct boundaries (Reiss et al., 2006; Hiesinger et al., 2012; Kneissl et al., 2014; Michael et al., 2016) or their rims (Baldwin, 1985).

* Corresponding author.
*E-mail address:* yuezy@radi.ac.cn (Z. Yue).

https://doi.org/10.1016/j.epsl.2021.117031

For several-km craters on the Moon, the transition from ejecta to the surrounding terrain is difficult to demarcate because the ejecta occur as a layer of continuously diminishing radial thickness. Moving away from the crater rim, it becomes more likely that a pre-existing crater remains observable, being merely draped by an ejecta layer of comparable or lesser thickness than its own relief. In general, such a crater may not be distinguishable from a more eroded crater atop the ejecta layer by means of images from orbit. In this work we constrain the measurement area more strictly to the uplifted rim, gaining the benefit of certainty of the erasure of pre-existing craters, and make use of a Poisson statistics analysis to maximize the information extracted from the small superposed crater population (Michael et al., 2016). It is expected that rim slopes could be problematic for crater counting because of mass-wasting processes and the preferential impact erosion which occurs there (Soderblom, 1970), both leading to increased crater loss. In this work we observe this effect for craters in roughly the upper 20 m of regolith; larger craters which substantially impinge the structure of the rim appear to withstand this erosion.

## 2. Method

The seven largest impact craters, of size 3–6 km, in the planned CE-5 landing region (49–69°W 41–45°N, Fig. 1) were selected for dating on a Lunar Reconnaissance Orbiter Narrow Angle Camera (LRO NAC) mosaic (Robinson et al., 2010; Di et al., 2019). For each crater, the Lunar Orbiter Laser Altimeter (LOLA)-Kaguya 512 pix/degree (∼60 m/pix) Digital Elevation Model (DEM) (Barker et al., 2016) was colourised such that the colour bar spans the height range from the local surrounding of the crater to the top of the crater rim. The area for crater counting was chosen as an annulus around the crater rim, its width being the limit of the area which is discernibly uplifted by the crater formation. In this area we are confident that any pre-existing crater structure would be fully obliterated. Although disruption of pre-existing craters may occur to a greater or lesser degree at larger distances, beyond the uplift we have no systematic way to determine whether a crater formed before or after the impact of interest.

The roughly 1 km diameter crater centred about 1.5 km NNW beyond the rim of crater 1 (Dechen B) indicated by a white arrow (Fig. 2a) appears to pre-date it with some of Dechen B's rim material covering its nearer edge. Had it formed marginally further away, this material would not be present, and the formation sequence unclear. On the other hand, it is unambiguous that the 650 m crater cutting the southern rim of crater 7 (Fig. 2c) post-dates it.

Such annuli were constructed for each crater of interest, and smaller craters occurring within or intersecting the annulus were identified and measured in NAC images down to a completeness limit of about 20 m diameter. Measurements were made using CraterTools (Kneissl et al., 2011) and overplotted on differential isochrons with Craterstats (Michael, 2013). At the same time, the largest craters of the region were used to estimate the average age of the main geological unit in the region in the conventional manner. We make use of the Neukum (1983) chronology model throughout, but the calculations could be adapted equivalently for alternative chronology systems.

## 3. Results

The crater populations of the seven rim-annuli are plotted in Fig. 3. Over the diameter range of 20–80 m, all are consistent with an isochron of <50 Ma in the Neukum (1983) chronology system. At the same time, the 14 largest craters (including six of those investigated) together suggest an age of $\mu 3.3^{+0.2}_{-0.4}$ Ga for the *Im2* unit (Qian et al., 2018), consistent with their finding of 3.39 Ga ($\mu$ is a function representing the uncertainty of calibration of the chronology model (Michael et al., 2016)).

If the annulus ages are interpreted to represent the formation times of their respective craters, the above results are not consistent. Since the six largest craters on *Im2* formed over a 3.3 Ga period, we should expect them to have formed with a spread of ages going back to the emplacement time of the surface. Instead, we see that all six formed within the last 50 Ma – only 1.5% of the history of the unit – which is vanishingly improbable. We therefore conclude that the annulus ages do not represent the crater formation times, but show the lifetime of the surface structure of the regolith to the depth of the superposed craters. From the largest of the size range, 80 m, we could estimate this depth to be around 20 m (Pike, 1974).

It is expected that rim slopes could be problematic for crater counting because of mass-wasting processes. The rim heights of the studied craters range from 80–320 m above the plateau, so a loss of structure in the upper 20 m may not be surprising.

Several annuli show superposed craters larger than 80 m. Although not in sufficient number to establish a clear isochron for any of the individual crater rims, in combination they show a scatter which suggests they could represent the accumulation population from formation. Crater 7 has the most at this scale, with 10.

If we aggregate together the data from the rim annuli of the *Im2* unit it becomes possible to estimate their *average* age, as was done previously for sets of wrinkle ridges showing only very few superposed craters (Yue et al., 2017). In that case, the aggregation was done with the belief that the selected ridge sets had a common origin, and that members of a given set would therefore have likely formed at similar times. Here, we have no such expectation: the craters should have formed at independently random times over the period since the emplacement of the *Im2* unit. Their average age, then, should reflect the average time since emplacement, which is around half the age of the unit (this is not exact, because the impact rate is higher in the interval 3–3.3 Ga). Fig. 4 shows this aggregation, where each annulus population has been normalised to 1 km$^2$ so that each contributes an equivalent weight to the total. Taking the population >250 m in diameter, we find an average age of $\mu 1.2^{+0.9}_{-0.9}$ Ga which, acknowledging the large error bars, is consistent with representing the half-age of the unit. In this case we use a least-squares fit to the differential production function rather than the Poisson approach because of the complication of the area normalisation.

## 4. Poisson calculation for a buffered area

In a previous work, the method for exact evaluation of a crater chronology model for use in the case of few superposed craters was presented (Michael et al., 2016). It was shown that the probability of observing a particular configuration of crater diameters, $\mathbb{D}$, after a time $t$ has elapsed is

$$\mathrm{pr}\left(\mathbb{D}, t\right) = \prod_{i=1}^{n} e^{-\lambda_i(t)} \prod_{d_i \in \mathbb{D}} \lambda_i\left(t\right) \tag{1}$$

where the measured diameter interval is divided into $n$ bins, and $n$ is sufficiently large that each crater falls into a separate bin. The average formation rate for craters in bin $i$ is,

$$\lambda_i(t) \approx AF\left(\overline{d}_i, t\right)\delta d \tag{2}$$

where $\overline{d}_i$ is the geometric mean diameter of interval $i$, and $A$ is the crater accumulation area and $F$ is the differential form of the production function (Arvidson et al., 1979). The form of $F(d)$

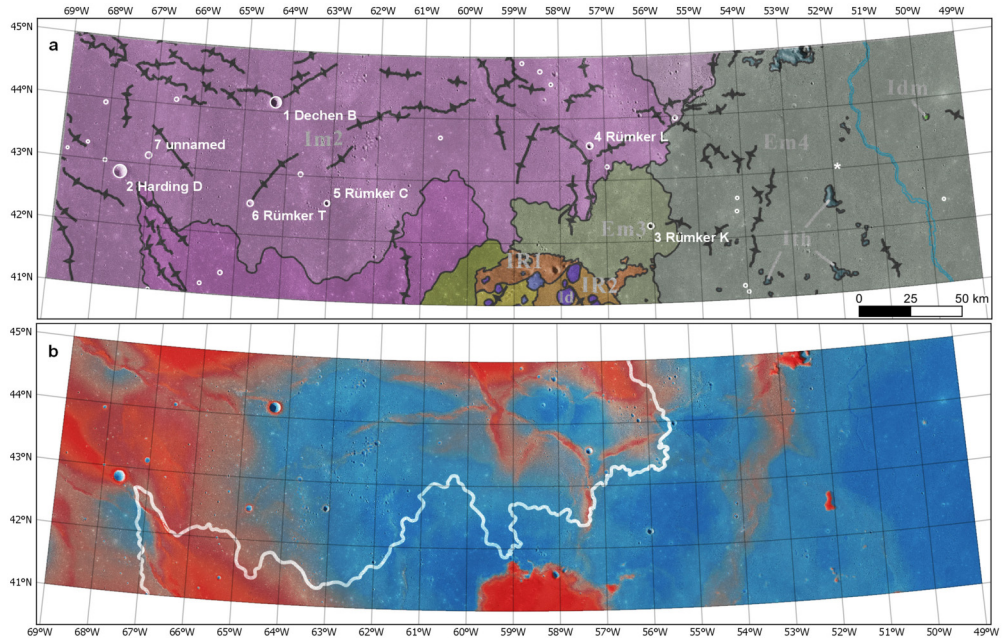


**Fig. 1.** Chang'E-5 planned landing region a) with seven dated craters indicated, over geologic mapping from Qian et al., 2018. Unit Im2 coloured mid-purple. Asterisk marks eventual landing location at 43.05°N, 51.92°W (added during revision). b) Same region shown as composite colourised DEM with Im2 boundary. (For interpretation of the colours in the figure(s), the reader is referred to the web version of this article.)

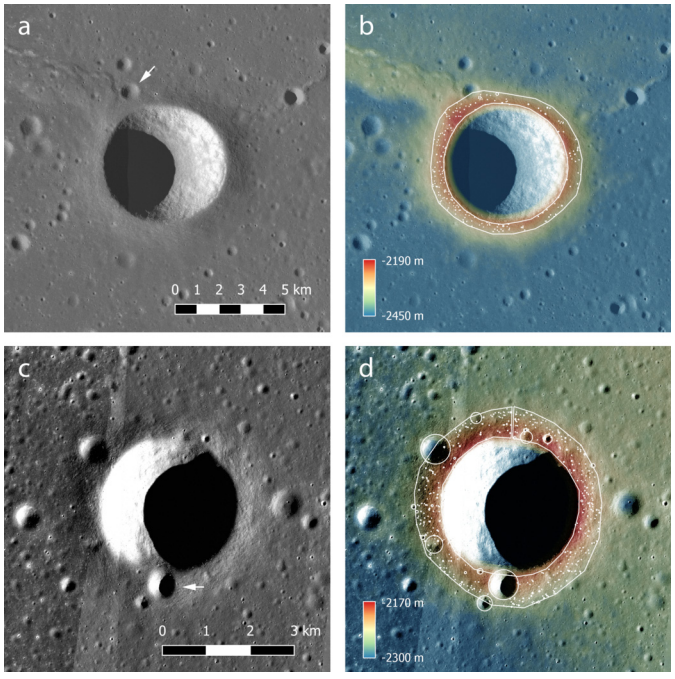


**Fig. 2.** Crater 1, Dechen B, seen in a) CE-5 NAC mosaic, b) colourised LOLA-Kaguya surface elevation. White line denotes region of elevated rim material, with superposed craters marked. c) Crater 7 (unnamed) showing larger superposed craters, and d) similarly with surface elevation.

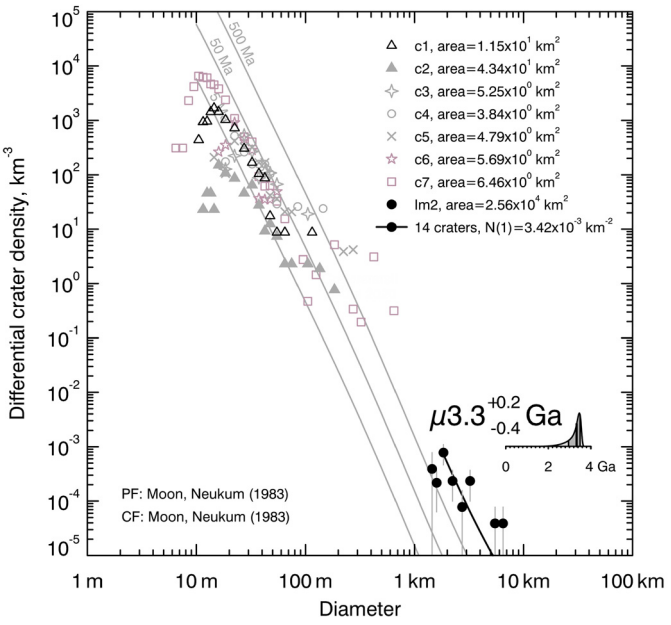


**Fig. 3.** Crater populations from annuli around the seven largest craters in the planned CE-5 landing region. Six of these and several smaller craters are used to estimate the age of the *Im2* unit (Qian et al., 2018) at $\mu 3.3^{+0.2}_{-0.4}$ Ga, where $\mu$ is a function representing the uncertainty of calibration of the chronology model (Michael et al., 2016).

for a Neukum-style polynomial production function was given in Michael and Neukum (2010) as their Eq. (3).

In Michael et al. (2016), Eq. (1) was evaluated in the limit of small intervals, taking the accumulation area $A$ to be of fixed size, permitting an evaluation of the chronology model to obtain a likelihood function for the age of a surface unit using a conventional crater count. For the crater annuli considered in this paper, a better estimate can be achieved using a buffered area crater count (Tanaka, 1982; Fassett and Head, 2008; Kneissl et al., 2015; Riedel et al., 2018). With this technique, not only craters which fall within the counting area are considered, but also those whose centres lie outside it while their rims still identifiably superpose the area. In this way, the effective counting area is increased, improving the statistics. The improvement increases as the counting area diminishes: in particular, the method may be applied to enable the dating of linear features such as ridges or channels with zero or near-zero area.

To make the equivalent Poisson calculation, we write the buffered area as a function of the superposed crater diameter, $d_i$,

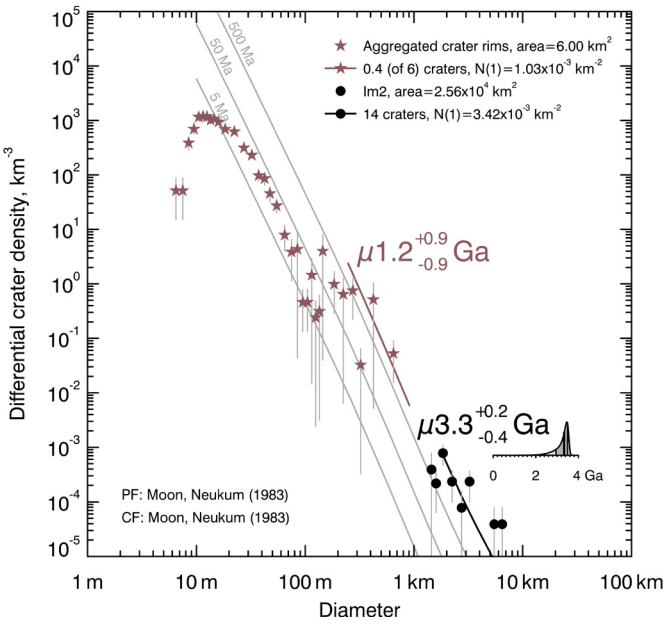


**Fig. 4.** Aggregated crater populations from rim annuli, each normalised to 1 km$^2$, around the six largest craters on the *Im2* unit of the planned CE-5 landing region. While the population below 100 m shows what we believe is a turnover age for the top 20 m of regolith of somewhat less than 50 Ma, the larger craters (here taking those >250 m) yield an average age for the six of $\mu 1.2^{+0.9}_{-0.9}$ Ga. Given that we expect that the average age of the six largest craters should be half of the age of the unit, this value is consistent with the hypothesis that annulus craters in this size range represent the accumulated populations since annulus formation.

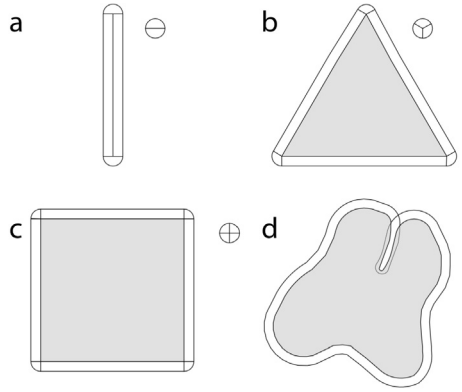


**Fig. 5.** The area of a buffer around a convex polygon depends on the length of the perimeter plus a circle of the buffer radius (see Equation (3)), illustrated here by a) a line feature, b) a triangle, c) a square. The same is true for mildly concave polygons, where the deficit of additional area from concave sections is cancelled out by the equivalent additional convex sections. However, if the concavity is sufficiently tight for d) self-intersection to occur in the buffer, the equation no longer holds.

$$A_i = A + \frac{d_i L}{2} + \frac{\pi d_i^2}{4} \tag{3}$$

where $A$ is the original counting area and $L$ – the length of its perimeter. The latter two terms represent the area of a buffer of width $d_i/2$ around a convex polygon. If we consider a square, it can be seen that they represent the buffered edges and the four quarter-circle rounded corners (Fig. 5c). The same expression holds for any other convex polygon, for single- or poly-line segments of zero area, and for mildly concave polygons. It begins to break down, however, when the concavity becomes sufficient that the buffer region becomes self-intersecting (Fig. 5d). For typically mapped counting areas, this will not usually be a concern.

Substituting Eq. (2) with the new form of $A_i$ into the first product of Eq. (1) gives

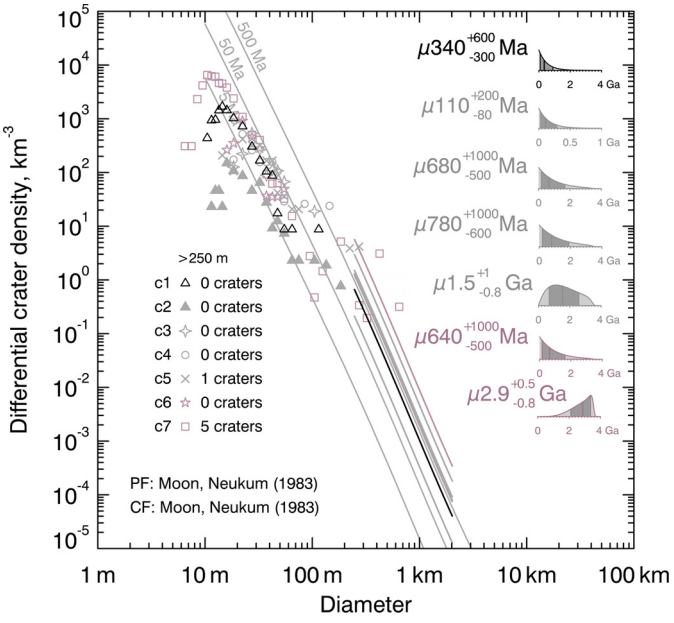


**Fig. 6.** Buffered Poisson calculation for craters 1 (upper inset plot) to 7 (lower). Inset plots show relative likelihood that crater has indicated age given observed superposed crater population. The 50 (median) and $50 \pm 34$ (1-sigma for a Gaussian distribution) percentiles are plotted and used to represent the model age and uncertainty numerically.

$$\lim_{n\to\infty}\left(\prod_{i=1}^{n} e^{-\lambda_i(t)}\right) = \exp\left(-\int_{d_{\min}}^{d_{\max}}\left(A + \frac{d_i L}{2} + \frac{\pi d_i^2}{4}\right) F(d,t)\,\mathrm{d}d\right)$$
$$= \exp\left(-If(t)\right)$$

There is no simple expression for the evaluation of the integral, but after removing the separable time dependence, $f(t)$, it can be evaluated numerically to give a constant, $I$. Removing all constant factors as previously, this leaves

$$\mathrm{pr}(\mathbb{D}, t) \propto \exp\left(-If(t)\right)\{f(t)\}^{n_{\mathbb{D}}} \tag{4}$$

choosing this time to express the result in terms of $f(t)$ instead of $C(d=1,t)$, since it appears in the exponent. The expression is equivalent to the previous formulation, the only difference being the increased magnitude of $I$.

Fig. 6 shows the result of applying the new expression (4) to the crater counts on the rim annuli. For craters 1, 2, 3, 4 and 6, there are no superposed craters in the >250 m size range. The likelihood functions therefore show a decreasing exponential form, and the 50$^{\text{th}}$ percentile represents the median time for the existence of an area of the given size without the formation of a >250 m crater. Crater 5 has one superposed crater of that size, while crater 7 has five. Their likelihood functions place their formation times in the mid and early history of the *Im2* unit respectively.

## 5. Discussion

The Apollo 15 landing site is a good example of a surface showing crater equilibrium (Minton et al., 2019). Their data shows a transition between the production and equilibrium curves occurring over the crater size range between about 70 and 150–180 m, depending on how the equilibrium curve is fit. This is for a surface dated at 3.54 Ga, so that we expect the equilibrium could extend to somewhat larger diameters than for the 3.3 Ga surface in this study. The portion of the equilibrium count in the same 20–80 m diameter range, for which we saw apparent 50 Ma isochrons, cuts

through isochrons in the range of roughly 150–1000 Ma. It is not unexpected that the equilibrium density on a slope should be considerably lower. Interestingly, the transition size to craters which carry meaningful age information is not very different.

Costello et al. (2018) predict that impact gardening generates at least one overturn of material to 1-2 m depth over a period of 1 Ga (their Fig. 9), which extrapolates to about 3 m over 3 Ga for a constant impact rate. On the slope of a crater rim, of course, much of any turnover is immediately lost downslope, exposing ever deeper material to the gardening flux. The same figure shows ten thousand turnovers to 10 cm depth for the same period. We think we are seeing loss of structure in the crater rims to 20 m depth over the course of 50 Ma. This period should correspondly see about 500 turnovers to 10 cm, and $10^4$ times more again to 1 cm. It is not hard to see that the loss per turnover does not need to be great to accumulate 20 m.

Fassett and Thomson (2014) suggested that, after 3 Ga, a 3 km crater only shows changes at the rim: this accords with the structure of the seven selected craters: even the oldest, crater 7, is well defined and retains 130 m of rim height. They also predict that a 300 m crater should be nearly imperceptible after the same period. There are two elements to the loss of perceptibility: the degradation of the rim – which happens relatively quickly in their model ($<$500 Ma for a 300 m crater) – and the infilling of the depression, which is slower. Their consideration was for craters forming on a horizontal surface: we expect the behaviour to be somewhat different for an impact into the rim of a several-km crater. The newly-formed rim likely degrades faster than for a typical crater because of being situated on a local slope. The infilling of the depression may be slowed because it is starved of material coming from the gravitational well that is the interior of the larger crater. However, more importantly, the criterion for imperceptibility changes: even after an equivalent amount of material has entered the depression, the interruption in the rim remains visible. This persists until most of the rim itself is eroded away, which is a much slower process. Du et al. (2019) estimated that a 5 km crater loses only about 45 m of rim height over 3.6 Ga, based on a topographic diffusivity of 5.5 $m^2$/Ma, which is only a small fraction of the rim heights we observe for the seven craters.

The asymmetry of ejection from a sloped target was considered by Soderblom (1970), who found that the most efficient erosion of a crater structure is produced by impacts forming craters around 10x smaller than the original. This is close to the onset size for craters carrying age information that we suggest here. At this size they transition to removing an amount of the rim which can no longer be covered over by topgraphic diffusion.

## 6. Conclusion

In conclusion we are, in a limited manner, able to estimate the ages of individual craters at 3–6 km scale using the annulus method from superposed craters in the $>$250 m size range, making use of the Poisson approach to extract the maximum timing information that is possible from the few craters which are present.

Although there are sufficient identifiable craters on rim-annuli of this scale in the 20–80 m size range to find a self-consistent isochron, this isochron is shown not to represent the age of the crater rim formation, but is rather interpreted to reflect the lifetime of regolith overturn to a depth of around 20 m. This lifetime appears to have an upper limit of around 50 Ma, which is about 10x less than for a horizontal surface (Minton et al., 2019), while at the same time being about 10x more than the overturn predicted for a horizontal surface (Costello et al., 2018). Both of these differences we attribute to the enhanced erosion on the rim slope.

If the Chang'E-5 soil samples prove to contain a datable impact melt component, the enumerated craters in this work are likely source candidates, with craters 3 & 4 (Rümker K, L) being the closest. The age likelihood functions derived for the craters studied here cover a broad range of values, such that, perhaps with the exception of crater 7, it would not be possible to deduce a direct connection from this information alone. Nevertheless, they provide the maximum timing information possible for any interpretations which are made.

We have demonstrated the application of Poisson statistics to analyse buffered crater counts, an approach which yields the maximum possible timing information from the data within a given chronology model. In particular, because of the low number of superposed craters typically present in a buffered count and the consequent problems for conventional data binning and isochron fitting or estimation, this method should be particularly beneficial to future studies of this type.

## CRediT authorship contribution statement

Gregory Michael: Conceptualization, Methodology, Software, Writing - Original draft preparation;
Zongyu Yue, Sheng Gou: Conceptualization, Writing.
Kaichang Di: Data

## Declaration of competing interest

The authors declare that they have no known competing financial interests or personal relationships that could have appeared to influence the work reported in this paper.

## Acknowledgements

This work was supported by the Strategic Priority Research Program of Chinese Academy of Sciences (grant No. XDB41000000), the German Space Agency (DLR Bonn), grants 50QM1702 (HRSC on Mars Express), on behalf of the German Federal Ministry for Economic Affairs and Energy, and by the German Research Foundation (DFG) SFB TRR-170-3 A3 and A4. We are grateful to David Minton and an anonymous reviewer for their comments which substantially improved the paper.

## References

Arvidson, R.E., Boyce, J., Chapman, C., Cintala, M., Fulchignoni, M., Moore, H., Neukum, G., Schultz, P., Soderblom, L., Strom, R., Woronow, A., Young, R., 1979. Standard techniques for presentation and analysis of crater size-frequency data. Icarus 37, 467–474.

Baldwin, R.B., 1985. Relative and absolute ages of individual craters and the rate of infalls on the Moon in the post-Imbrium period. Icarus 61, 63–91.

Barker, M.K., Mazarico, E., Neumann, G.A., Zuber, M.T., Haruyama, J., Smith, D.E., 2016. A new lunar digital elevation model from the Lunar Orbiter Laser Altimeter and SELENE Terrain Camera. Icarus 273, 346–355.

Costello, E.S., Ghent, R.R., Lucey, P.G., 2018. The mixing of lunar regolith: vital updates to a canonical model. Icarus 314, 327–344.

Di, K., Jia, M., Xin, X., Wang, J., Liu, B., Li, J., Xie, J., Liu, Z., Peng, M., Yue, Z., Liu, J., Chen, R., Zhang, C., 2019. High-resolution large-area digital orthophoto map generation using LROC NAC images. Photogramm. Eng. Remote Sens. 85, 481–491.

Du, J., Fa, W., Wieczorek, M.A., Xie, M., Cai, Y., Zhu, M.-H., 2019. Thickness of lunar mare basalts: new results based on modeling the degradation of partially buried craters. J. Geophys. Res., Planets 124, 2430–2459.

Fassett, C.I., Head, J.W., 2008. The timing of martian valley network activity: constraints from buffered crater counting. Icarus 195, 61–89.

Fassett, C.I., Thomson, B.J., 2014. Crater degradation on the lunar maria: topographic diffusion and the rate of erosion on the Moon. J. Geophys. Res., Planets 119, 2255–2271.

Hiesinger, H., van der Bogert, C.H., Pasckert, J.H., Funcke, L., Giacomini, L., Ostrach, L.R., Robinson, M.S., 2012. How old are young lunar craters? J. Geophys. Res., Planets 117 (E12). https://doi.org/10.1029/2011JE003935.

Kirchoff, M.R., Chapman, C.R., Marchi, S., Curtis, K.M., Enke, B., Bottke, W.F., 2013. Ages of large lunar impact craters and implications for bombardment during the Moon's middle age. Icarus 225, 325–341.

Kneissl, T., van Gasselt, S., Neukum, G., 2011. Map-projection-independent crater size-frequency determination in GIS environments–new software tool for ArcGIS. Planet. Space Sci. 59, 1243–1254.

Kneissl, T., Michael, G.G., Platz, T., Walter, S.H.G., 2015. Age determination of linear surface features using the Buffered Crater Counting approach - Case studies of the Sirenum and Fortuna Fossae graben systems on Mars. Icarus 250, 384–394.

Kneissl, T., Schmedemann, N., Reddy, V., Williams, D.A., Walter, S.H.G., Neesemann, A., Michael, G.G., Jaumann, R., Krohn, K., Preusker, F., Roatsch, T., Corre, L.L., Nathues, A., Hoffmann, M., Schäfer, M., Buczkowski, D., Garry, W.B., Yingst, R.A., Mest, S.C., Russell, C.T., Raymond, C.A., 2014. Morphology and formation ages of mid-sized post-Rheasilvia craters – Geology of quadrangle Tuccia, Vesta. Icarus 244, 133–157.

Michael, G.G., 2013. Planetary surface dating from crater size-frequency distribution measurements: multiple resurfacing episodes and differential isochron fitting. Icarus 226, 885–890.

Michael, G.G., Kneissl, T., Neesemann, A., 2016. Planetary surface dating from crater size-frequency distribution measurements: Poisson timing analysis. Icarus 277, 279–285.

Michael, G.G., Neukum, G., 2010. Planetary surface dating from crater size–frequency distribution measurements: partial resurfacing events and statistical age uncertainty. Earth Planet. Sci. Lett. 294, 223–229.

Minton, D.A., Fassett, C.I., Hirabayashi, M., Howl, B.A., Richardson, J.E., 2019. The equilibrium size-frequency distribution of small craters reveals the effects of distal ejecta on lunar landscape morphology. Icarus 326, 63–87.

Neukum, G., 1983. Meteoritenbombardement und Datierung planetarer Oberflachen (English translation, 1984: Meteorite bombardment and dating of planetary surfaces). http://ntrs.nasa.gov/search.jsp?R=19840027189.

Pike, R.J., 1974. Depth/diameter relations of fresh lunar craters - revision from spacecraft data. Geophys. Res. Lett. 1, 291–294.

Qian, Y.Q., Xiao, L., Zhao, S.Y., Zhao, J.N., Huang, J., Flahaut, J., Martinot, M., Head, J.W., Hiesinger, H., Wang, G.X., 2018. Geology and scientific significance of the Rümker region in Northern Oceanus Procellarum: China's Chang'E-5 landing region. J. Geophys. Res., Planets 123, 1407–1430.

Reiss, D., Gasselt, S., Hauber, E., Michael, G., Jaumann, R., Neukum, G., 2006. Ages of rampart craters in equatorial regions on Mars: implications for the past and present distribution of ground ice. Meteorit. Planet. Sci. 41, 1437–1452.

Riedel, C., Michael, G., Kneissl, T., Orgel, C., Hiesinger, H., van der Bogert, C.H., 2018. A new tool to account for crater obliteration effects in crater size-frequency distribution measurements. Earth Space Sci. 5, 258–267.

Robinson, M.S., Brylow, S.M., Tschimmel, M., Humm, D., Lawrence, S.J., Thomas, P.C., Denevi, B.W., Bowman-Cisneros, E., Zerr, J., Ravine, M.A., Caplinger, M.A., Ghaemi, F.T., Schaffner, J.A., Malin, M.C., Mahanti, P., Bartels, A., Anderson, J., Tran, T.N., Eliason, E.M., McEwen, A.S., Turtle, E., Jolliff, B.L., Hiesinger, H., 2010. Lunar Reconnaissance Orbiter Camera (LROC) Instrument Overview. Space Sci. Rev. 150, 81–124.

Soderblom, L.A., 1970. A model for small-impact erosion applied to the lunar surface. J. Geophys. Res. 75, 2655–2661.

Tanaka, K.L., 1982. A new time-saving crater-count technique, with application to narrow features. NASA Technical Memo, NASA TM-85127.

Yue, Z., Michael, G.G., Di, K., Liu, J., 2017. Global survey of lunar wrinkle ridge formation times. Earth Planet. Sci. Lett. 477, 14–20.

Zhao, J., Xiao, L., Qiao, L., Glotch, T.D., Huang, Q., 2016. The Mons Rümker volcanic complex of the Moon: a candidate landing site for the Chang'E-5 mission. J. Geophys. Res., Planets 122, 1419–1442.

Zou, Y.L., Li, W., 2017. Scientific visions of lunar research-station from China. In: Lunar Planetary Science Conference, Lunar Planetary Science Conference, p. 1730.